Titre: Title:	Introduction and implementation of fluid forces in a DEM code for simulating particle settlement in fluids
Auteurs: Authors:	Yuyu Zhang, & Li Li
Date:	2024
Type:	Article de revue / Article
Référence: Citation:	Zhang, Y., & Li, L. (2024). Introduction and implementation of fluid forces in a DEM code for simulating particle settlement in fluids. Powder Technology, 119238 (18 pages). https://doi.org/10.1016/j.powtec.2023.119238

Introduction and implementation of fluid forces in a DEM code for simulating particle settlement in fluids

Yuyu Zhang[1*], and Li Li[2]

[1]Ph.D. Student

Research Institute of Mines and Environment (RIME UQAT-Polytechnique)

Department of Civil, Geological and Mining Engineering

Polytechnique Montréal

C.P. 6079, Succursale Centre-Ville, Montréal, Québec, Canada, H3C 3A7

E-mail: yuyu.zhang@polymtl.ca

[2]Full Professor, Ph.D.

Research Institute of Mines and Environment (RIME UQAT-Polytechnique)

Department of Civil, Geological and Mining Engineering

Polytechnique Montréal

C.P. 6079, Succursale Centre-Ville, Montréal, Québec, Canada, H3C 3A7

E-mail: li.li@polymtl.ca

*Corresponding author: Yuyu Zhang; E-mail: yuyu.zhang@polymtl.ca

Submitted to and accepted by *Powder Technology*

* Corresponding author. E-mail: yuyu.zhang@polymtl.ca

Introduction and implementation of fluid forces in a DEM code for simulating particle settlement in fluids

Abstract:

Simulations of a problem involving particles and fluid usually require coupling a discrete element method (DEM) with computational fluid dynamics (CFD) or smoothed particle hydrodynamics (SPH). The former suffers from the accuracy or even reliability problem induced by mesh size while the latter suffers from small size model and high computation time and cost. To overcome part of these problems, fluid forces have been formulated and directly implemented in a DEM code, resulting in a new model, named f-EDEM. Using this model, the settlement of particles in a fluid can be simulated by a single DEM code without the need of coupling with a CFD or SPH solver. In this study, the formulation and implementation of fluid forces into the DEM code are presented. The proposed f-EDEM model is first validated against an analytical solution. The applicability and ability of the f-EDEM model are examined by reproducing and predicting some laboratory results. The comparisons between the numerical, analytical and experimental results indicate that the f-EDEM model is successfully validated and has the required capacity for simulating the settlement of single and multiple particles in both Newtonian and some of non-Newtonian (Bingham plastic) fluids. The results also indicate that the time step recommended by most DEM manuals can be excessively small, resulting in a high computational cost. It is thus necessary to perform sensitivity analysis of time step to obtain an optimal numerical model, which ensures stable and reliable numerical result with the shortest time of computation.

Keywords: Discrete element method (DEM); Particle settlement; Bingham plastic fluids; Fluid forces.

1. Introduction

Particle settlement in fluids is a phenomenon frequently encountered in several domains, such as mineral slurries, debris flows, natural muds, landslides, and lava flows (Bokharaeian et al., 2021; Nguyen et al., 2021). Understanding and quantifying the particles settlement is thus necessary for the design and control of such systems. Obviously, this should be extremely difficult, if not totally impossible through analytical solution due to the large number of particles and the extremely complex interactions between particles and particles as well as between particles and fluid. Alternatively, numerical modeling can be considered as a versatile way to evaluate the interaction between particles and fluid.

There are two major numerical approaches that can be employed to simulate the movement of particles in fluids. The first one couples discrete element method (DEM) with computational fluid dynamics (CFD) method. The movement of an individual particle is explicitly tracked by solving the Newton's second law using DEM (Cundall & Strack, 1979), while the flow of fluid is described by the Navier-Stokes equation in CFD (Fonceca Junior et al., 2021; Jajcevic et al., 2013; Tsuji et al., 1993; Zhao & Shan, 2013). The fluid related forces such as drag and buoyance forces are calculated by the CFD solver and then taken as input parameters for the DEM code. This approach has been applied to simulate gas-solid fluidization, pneumatic conveying, cyclones and pipeline flow (Picabea et al., 2022; Zhao & Shan, 2013; Zhu et al., 2008). The approach (un-resolved DEM-CFD method), however, can become problematic with large size particles because the CFD mesh size must be larger than the maximum diameter of particles (Casarin et al., 2022; Ferreira et al., 2023; Kloss et al., 2012; Peng et al., 2014; Zhang & Yin, 2018). The requirement may result in overly coarse CFD meshes when simulating particles containing very large ones. The accuracy reduces and the numerical results can become unreliable. Moreover, the strong interaction processes (e.g., transport fluid forces from CFD to DEM) between the two codes can sometimes contribute to numerical instabilities (Casarin et al., 2022). In addition, for a simple one-way simulation (only the fluid affects the flow of particles), the velocity fields data calculated by the CFD solver can be imported into some DEM codes. This allows the movement of particles induced by the fluid to be captured in DEM but does not necessarily require coupling the two codes at the same time. At current state, several commercial DEM codes can support this approach to different levels of complexity (e.g., Altair EDEM, Ansys Rocky, ThreeParticle).

The second approach is to couple DEM with the smoothed particle hydrodynamics (SPH) method. SPH is a mesh-free method, in which the fluid is discretized into a set of particles (Gingold & Monaghan, 1977; Platzer & Fimbinger, 2021) to simulate complicated free-surface flow and splashing without any problem of convergences (Cleary & Prakash, 2004; Cleary et al., 2006; He et al., 2018; Moreira et al., 2020; Peng et al., 2021; Robb et al., 2016; Wu et al., 2020). The coupled DEM-SPH method has thus been majorly used to simulate the free flows, such as debris flows, landslides and dam breaks (Cleary, 2015; Robinson et al., 2013; Trujillo-Vela et al., 2020; Zhou & Li, 2022). However, application of coupled DEM-SPH method is limited to small scale engineering problems due to the extremely high computational time and costs. In each simulation step of SPH method, the neighboring particles must be searched and their effects on the current particle must be taken into account. Such search and update calculations require enormous computation time when simulating the fluid represented by large quantities of particles (Domínguez et al., 2021; Ohno et al., 2017; Park et al., 2020; Valdez-Balderas et al., 2013). Once the SPH solver needs to be coupled with DEM, the calculation time can further increase significantly due to the additional particles associated with the DEM code.

The previous analysis on existing numerical methods elucidates that coupling two different numerical codes may suffer from a problem of numerical stability/reliability or from a problem of computation time/cost when dealing with the movement of particles in a fluid. In order to overcome (at least partly) these problems, a new component has been developed and implemented on a commercialized DEM code, after taking into account the drag and buoyance forces of fluid. The settlement of particles in both Newtonian and some non-Newtonian (e.g., Bingham plastic) fluids can thus be simulated using a single DEM code without any need of coupling with a CFD or SPH solver. In this study, the development is presented. The developed numerical model is validated against an analytical solution. The applicability and power of the numerical model is tested by the reproduction and prediction of experimental results.

2. Governing equations and forces

In this study, a DEM based commercial software, named Altair EDEM was used for numerical simulations. In DEM code, the translational and rotational accelerations of a particle are ruled by Newton's second law. The velocity and position of an individual particle are calculated and updated through numerical integration over a considered time step. The governing equation, which

104 controls the movement of a particle in a fluid, is expressed as the following equation based on the
105 DEM theory proposed by Cundall & Strack (1979):

$$m\frac{dv}{dt} = F_g + F_c + F_f \quad (1)$$

106 where m and v are the mass and translational velocity of the particle, respectively; t is time; F_g is
107 the gravitational force; F_c is the contact force between particles; F_f are the fluid forces acting on
108 the particles (presented later).

109 The rotation motion of a particle is described as follows (Cundall & Strack, 1979):

$$I\frac{dw}{dt} = M \quad (2)$$

110 where I is the moment of inertia, w is the angular velocity, M is the contact torque acting on a
111 particle.

112 The gravity force, F_g, acting on a spherical particle is expressed as follows:

$$F_g = \frac{1}{6}\pi\rho_p d^3 g \quad (3)$$

113 where ρ_p is the density of particle, d is the diameter of particle, g is the acceleration of gravity.

114 The contact forces, F_c, between particles are determined based on Hertz-Mindin (H-M) contact
115 model due to its accuracy and efficiency in contact force calculations (Hertz, 1882; Mindlin, 1949).
116 Particles are assumed to be rigid. Small overlaps are allowed to represent particle deformations
117 during collisions. By using contact detection algorithms, the accelerations, velocities and positions
118 of particles can be calculated using Newton's second laws of motion. More details on contact
119 forces of the H-M model can be found in many references (e.g., Capozzi et al., 2019; Dhaouadi et
120 al., 2021; Salamat & Genç, 2023).

121 In DEM code, the gravity force and contact force have often been taken into account and built in,
122 whereas the fluid forces, F_f (in Equation 1), are not incorporated because the fluid is not considered.
123 In this study, interaction between particles and fluid are concerned and the fluid forces are taken
124 into account by considering buoyance force and drag force.

125 The buoyance force F_b acting on a spherical particle fully submerged in a fluid can be expressed
126 by considering the Archimedes' principle as follows (Britannica, 2023):

$$F_b = \frac{1}{6}\pi\rho_f d^3 g \tag{4}$$

where ρ_f is the density of fluid.

Regarding the drag force, one has to consider if the fluid is a Newtonian fluid or non-Newtonian fluid. In a Newtonian fluid, the general form of drag force acting on a spherical particle settling in the fluid can be expressed as (Di Felice, 1994):

$$F_d = \frac{1}{2}\rho_f v^2 A C_d \tag{5}$$

where F_d is the drag force; v is the settling velocity of particle; A (= $\pi d^2/4$) is the cross-section area of a spherical particle; C_d is a drag coefficient, which depends on the shape and surface state of the particle and on the particle Reynolds number R_e, is expressed as follows (Chhabra, 2006; Okesanya et al., 2020):

$$R_e = \frac{\rho_f v d}{\eta} \tag{6}$$

where η is the viscosity of a Newtonian fluid.

For a spherical particle settling in a laminar flow region with very small Reynolds number, the drag force can be expressed based on Stokes law (Stokes, 1844):

$$F_d = 3\pi\eta v d \tag{7}$$

Substituting equation (7) into (5), one can obtain the relationship between the drag coefficient and Reynolds number of a sphere in stokes flow (Concha Arcil, 2009):

$$C_d = \frac{24}{R_e} \tag{8}$$

For the drag force of a spherical particle in a non-Newtonian fluid with a yield stress, the influence of yield stress must be considered. The drag force acting on a moving spherical particle in such fluid is given by Dedegil (1987) as follows:

$$F_d = (\frac{\pi}{2}d)^2\tau_y + \frac{1}{2}C_d\rho_f v^2 A \tag{9}$$

where τ_y is the yield stress, which is the minimum required shear stress to start flowing a non-Newtonian fluid.

The Reynolds number of particle in a non-Newtonian fluid can be expressed as follows after a generalization of Equation (6) for Newtonian fluid (Dedegil, 1987; Machač et al., 1995):

$$R'_e = \frac{\rho_f v d}{\eta_a} \tag{10}$$

where R'_e is the particle Reynolds number in a non-Newtonian fluid; η_a is the apparent viscosity of a non-Newtonian fluid, determined as the slope of shear stress, τ, and shear rate, $\dot{\gamma}$, as follows (He et al., 2001):

$$\eta_a = \frac{\tau}{\dot{\gamma}} \tag{11}$$

The particle to fluid shear rate, $\dot{\gamma}$, is defined as follows (Dedegil, 1987; He et al., 2001):

$$\dot{\gamma} = \frac{v}{d} \tag{12}$$

In this study, the non-Newtonian fluid with a yield stress is considered as a Bingham plastic fluid with its shear stress τ is described by the Bingham model (Blackery & Mitsoulis, 1997):

$$\tau = \tau_y + \eta_B \frac{v}{d} \tag{13}$$

where η_B is the plastic viscosity of a Bingham fluid.

Substituting equations (11), (12), (13) into equation (10) results in an expression for the particle Reynolds number of a sphere in a Bingham plastic fluid as follows (Dedegil, 1987):

$$R'_e = \frac{\rho_f v^2}{\left[\tau_y + \eta_B (\frac{v}{d})\right]} \tag{14}$$

To establish a relationship between the drag coefficient, C_d, and Reynolds number, R'_e of a particle in a Bingham plastic fluid, the settlement of a particle in such fluid is analyzed. When a particle is released into the fluid, its velocity increases upon the influence of gravity, a constant buoyance force, and a small but increasing drag force associated with the increasing velocity of settlement. The acceleration of settlement decreases as the sinking velocity and associated drag force increase. The sinking velocity reaches a maximum and constant value, usually called terminal velocity, when an equilibrium is achieved between the gravity force, the buoyance, and drag forces:

$$F_b + F_d - F_g = 0 \tag{15}$$

Substituting equations (3), (4) and (9) into equation (15) leads to:

$$\frac{1}{6}\pi\rho_p d^3 g - \frac{1}{6}\pi\rho_f d^3 g - \left(\frac{\pi}{2}d\right)^2 \tau_y - \frac{1}{2}C_d\rho_f v_{ter}^2 A = 0 \tag{16}$$

where v_{ter} is the terminal velocity of a particle settling in a fluid; A is the cross-section area of a spherical particle.

The drag coefficient of a particle can then be expressed as follows:

$$C_d = \frac{2}{v_{ter}^2\rho_f}\left[\frac{2}{3}(\rho_p - \rho_f)dg - \pi\tau_y\right] \tag{17}$$

Substituting the velocity v of equation (14) by the terminal velocity v_{ter} leads to an expression for the particle Reynolds number R'_e as follows:

$$R'_e = \frac{\rho_f v_{ter}^2}{\left[\tau_y + \eta_B\left(\frac{v_{ter}}{d}\right)\right]} \tag{18}$$

A relationship between C_d and R'_e can then be established through the terminal velocity v_{ter} included in both of equations (17) and (18). In this study, the $C_d - R'_e$ relationship is determined based on the test results of Valentik & Whitmore (1965), who conducted spheres settling tests in clay suspensions. The tests were realized with 121 spheres settling in clay suspensions having six different densities. The terminal velocity v_{ter} of each sphere in the clay suspension was well recorded. Fig. 1 shows the variation of drag coefficient C_d of each sphere at its terminal velocity as a function of the corresponding particle Reynolds number R'_e.

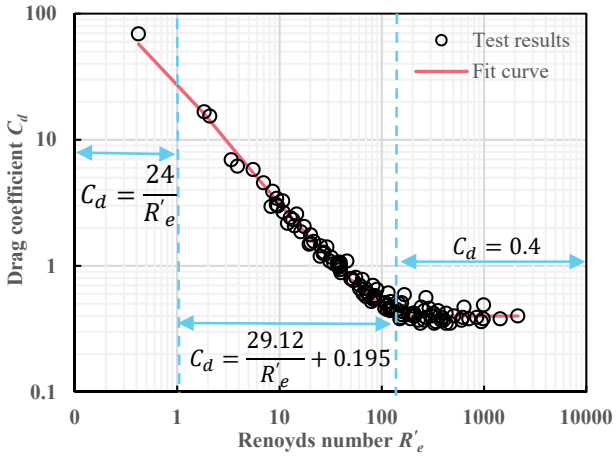

Fig. 1 Variation of drag coefficient C_d as a function of the corresponding particle Reynolds number R'_e of each sphere with the settling test results of Valentik & Whitmore (1965)

Applying the curve-fitting technique on the test results shown in Fig. 1 leads to a $C_d - R'_e$ relationship for sphere settling in clay suspensions as follows:

$$C_d = \begin{cases} \dfrac{24}{R'_e}, & R'_e < 1 \\ \dfrac{29.12}{R'_e} + 0.195, & 1 \le R'_e \le 150 \\ 0.4, & R'_e > 150 \end{cases} \tag{19}$$

This equation will be used to describe the $C_d - R'_e$ relationship for spheres settling in a Bingham plastic fluid. It should be noted here, the proposed $C_d - R_e'$ relationship (equation (19)) is different from the one proposed by Dedegil (1987). This is because the shear stress τ used by Dedgil (1987) is taken from the shear stress and shear rate curve conducted by Valentik & Whitmore (1965). However, in this study, the shear stress τ is applied based on Bingham model (equation (13)) which leads to the difference of the particle Reynolds number R_e'.

3. Implementation and validation of the f-EDEM model

As mentioned, this work is developed based on a commercialized DEM code, named Altair EDEM. An advantage of this code is the possibility of introducing user-defined-force-models, external couplings and particle-generation factories through API (standing for Application Programming Interface). To implement the fluid forces into EDEM, the buoyance force (equation (4)) and drag force (equations (5) and (9)) were translated and compiled into a DLL (standing for Dynamic Loading Library) module through Visual Studio C++ programming. The DLL module can be loaded and run by EDEM to take into account the fluid forces as plug-in particle body forces (Fig. 2). In the simulation, the fluid forces are automatically applied to the particles once they enter inside the pre-determined fluid area. This development results in a new model, named f-EDEM for modeling particle settlement in fluids.

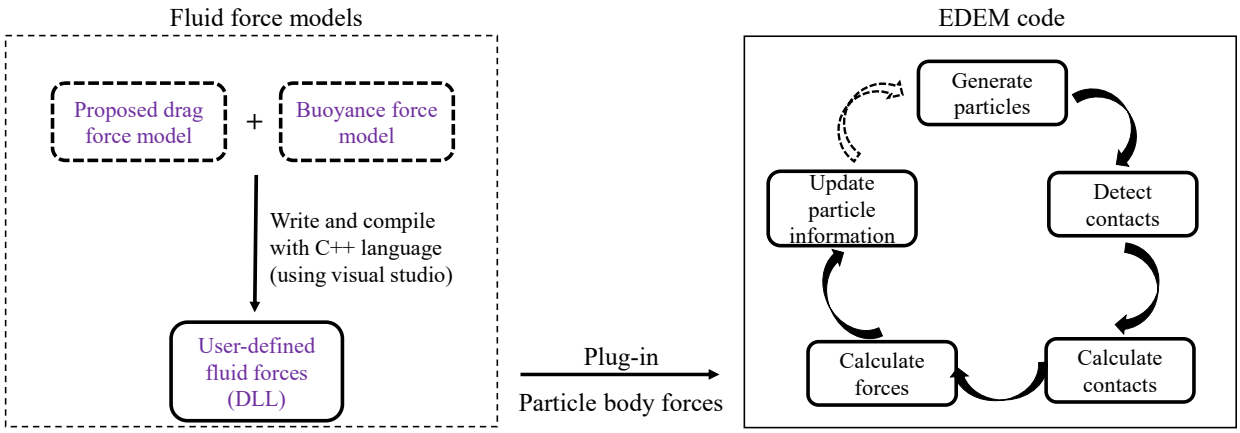

198

199 **Fig. 2** Flowchart of fluid forces programming and implementation in EDEM

200 Before any applications of a numerical model, the validation against analytical solutions must be
201 done in order to ensure that the numerical code does not contain any errors and the user can
202 correctly use the numerical code (Li, 2022). To do so, both of the numerical model and physical
203 model should not contain any uncertainty. In this regard, the comparison between numerical and
204 experimental results to obtain a good agreement, usually through the process of calibration (i.e.,
205 adjustment of some parameters), is not a validation because the experiment results contain always
206 more or less uncertainty. No one can guarantee whether the calibrated parameters are reliable or
207 unreliable. The comparisons are thus a process of calibration, useful to test the applicability or
208 power of the numerical model, but questionable as a validation of the numerical model (Li, 2022).

209 In this study, the validation of the f-EDEM model will be done against the settlement of a single
210 spherical particle in water. Fig. 3 presents the physical model of a spherical particle, settling down
211 in water with an initial speed of zero. The drag force acting on the particle is expressed by Stokes
212 drag (equation (7)), the settlement of the spherical particle in water is thus governed by the
213 following equation (Zhao et al., 2014):

$$\frac{1}{6}\pi d^3\rho_p\frac{dv}{dt}=\frac{1}{6}\pi d^3\left(\rho_p-\rho_w\right)g-3\pi d\mu_w v \tag{20}$$

214 where d is the diameter of particle, ρ_p is the density of particle, ρ_w is the density of water, μ_w is the
215 viscosity of water, v is the settling velocity of the particle.

216 Integrating equation (20) and considering the initial condition of $v=0$ at $t=0$ lead to an expression
217 for the terminal velocity of particle v_{ter} as follows (Stokes, 1844; Concha Arcil, 2009):

$$v_{ter} = \frac{d^2(\rho_p - \rho_w)g}{18\mu_w} \tag{21}$$

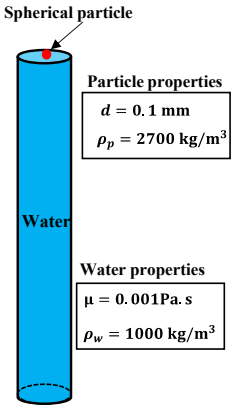

Fig. 3 Physical model of the settlement of a spherical particle in the water

The validation of the f-EDEM model is realized by considering the physical parameters given in Table 1.

Table 1 Physical parameters and considered time for the settlement of a spherical particle in water

Particle diameter, d_p (mm)	0.1
Particle density, ρ_p (kg/m^3)	2700
Poisson's ratio of particle, ν	0.25
Young's modulus of particle, E (GPa)	30
Water density, ρ_w(kg/m^3)	1000
Water viscosity, μ_w (Pa. s)	0.001

Fig. 4 presents the numerical model of the physical model presented in Fig. 3, built with EDEM by considering the physical parameters given in Table 1.

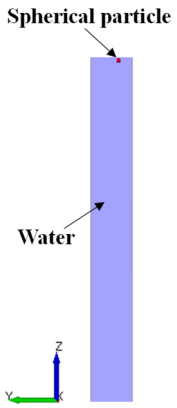

Fig. 4 Numerical model of Fig. 3 by considering the physical parameters given in Table 3, built with EDEM

In order to obtain stable and reliable numerical results, sensitivity analysis of time step is necessary. In this regard, a time step equaling to 10 to 20% of the Rayleigh time T_R is commonly recommended in DEM simulations (Washino et al., 2016). The Rayleigh time T_R is expressed by the following equation (Li et al., 2005; Rackl & Hanley, 2017; Burns et al., 2019):

$$T_R = \frac{\pi r_p}{0.8766 + 0.163\,\nu}\sqrt{\frac{\rho_p}{G}} \tag{22}$$

where r_p is the particle radius, ν is the Poisson's ratio of particle, ρ_p is the particle density, G is the shear modulus of particle. Considering the physical parameters given in Table 3 with $r_p = d_p/2$ = 0.1 mm/2 = 0.05 mm and $G = \frac{E}{2(1+\nu)}$ = 12 GPa and applying equation (22) lead to a value of T_R = 8.12×10^{-8} s. With 20% of T_R, the recommended time step is 1.62×10^{-8} s.

Fig. 5 presents the variation of the settling velocity of the particle at t = 0.001 s as a function of time step. One sees that the numerical results become stable when the time step is smaller than 2.5×10^{-5} s. The numerical results do not change any more significantly as the time step further decreases. The optimal time step is thus around 2.5×10^{-5} s; a value of 1.0×10^{-5} s was taken to be somehow conservative. These values are much larger than the time step of 1.62×10^{-8} s, recommended and commonly used in DEM simulations (20% of T_R). For such case, the application of the recommended and commonly used time step can result in unnecessary costs of simulation time. For a much more complicated situation with much more particles, it is unknown if the time step determined by using 20% of T_R is too large or too small. The former case results in instable

and unreliable numerical results while the latter case generates useless waste of time and cost calculations. None of them is desirable. The good and reliable way is to always conduct sensitivity analysis of time step, case by case, to find the optimal time step in order to ensure stable and reliable numerical result with the shortest time of calculations.

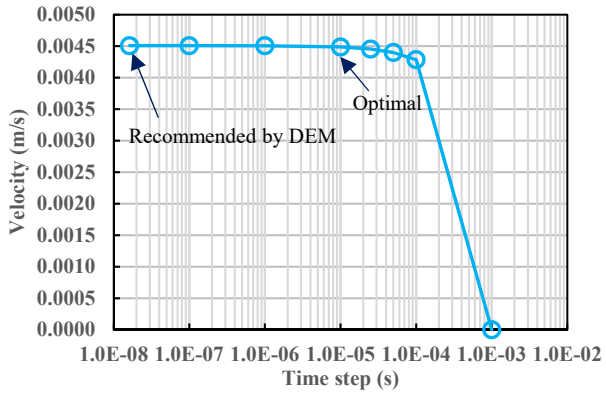

Fig. 5 The variation of settling velocity (t = 0.001 s) of spherical particle as a function of time step

Fig. 6 presents the variation of settling velocity of the particle in the water with time, obtained by applying the analytical solution (Equation (20)) and numerical model with the optimal time step of 1×10^{-5} s. A perfect agreement is obtained between the analytical and numerical results. The f-EDEM model can thus be considered as validated by the analytical solution. It remains to test the applicability or power of the numerical model against experimental results.

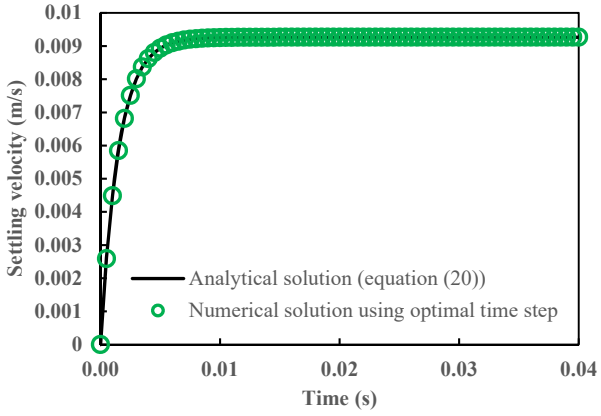

Fig. 6 Variation of settling velocity of the particle as a function of time, obtained by applying the analytical solution (Equation (20)) and f-EDEM model with the optimal time step of 1×10^{-5} s

4. Application and ability of the f-EDEM model

In this section, the f-EDEM model is employed to reproduce and predict the experimental results regarding the settlement of particles in different fluids. The applicability and ability of the f-EDEM model are examined by comparing the numerical results with the laboratory results.

4.1. Application of the f-EDEM model to numerically reproduce the tests of spheres settling in clay suspensions

In this part, the applicability or power of the f-EDEM model is tested by reproducing and predicting the experimental results obtained by Valentik & Whitmore (1965), who conducted several tests of spheres settling in clay suspensions. Fig. 7 shows a schematic presentation of the physical model used by Valentik & Whitmore (1965) for testing the settlement of a sphere in clay suspensions. The clay suspensions were poured in a vertical tank of 3 m high. A sphere was released from a vacuum tube into the clay suspension. The terminal velocity of the sphere in the suspension was recorded using detectors fixed outside the tank. The diameters of spheres range from 9.5 to 57 mm and their densities were changed by adding fine lead shot to a sealed opening in the sphere.

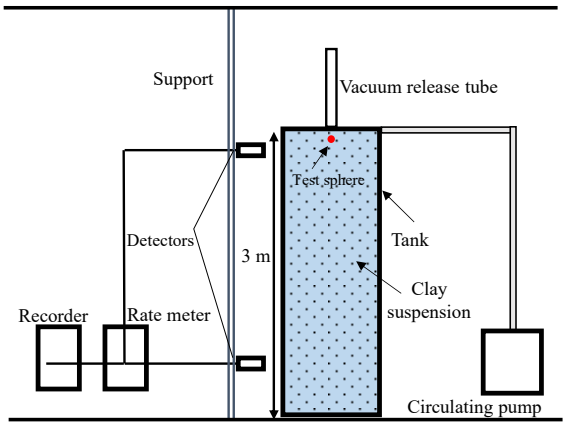

Fig. 7 A schematic presentation of the physical model of Valentik and Whitmore (1965) for testing the settlement of a sphere in clay suspensions

The detailed physical parameters for the clay suspensions and the corresponding particle Reynolds number R'_e as well as the drag coefficient C_d of spheres are shown in Tables 2 and 3, respectively.

Table 2 Physical parameters of clays suspensions used in the tests (Valentik & Whitmore, 1965)

	Density $\rho_{\_clay}$ (kg/m^3)	Plastic viscosity η_B (Pa. s)	Yield stress τ_y (Pa)
Clay suspension 1	1280	0.0131	30.5
Clay suspension 2	1254	0.0095	22.5
Clay suspension 3	1226	0.0081	17.5
Clay suspension 4	1207	0.0067	13
Clay suspension 5	1184	0.0054	8.5
Clay suspension 6	1149	0.004	4

281

282 **Table 3** Physical parameters of spheres and the corresponding particle Reynolds number R'_e and drag
283 coefficients C_d by applying equations (18) and (17), respectively

	Diameter of sphere $d_{\_sphere}$ (m)	Density of sphere $\rho_{\_sphere}$ (kg/m^3)	Terminal velocity v_{ter} (m/s)	Particle Reynolds number R'_e	Drag coefficient C_d
Suspension 1	0.0159	6450	0.1	0.42	69.03
	0.019	5832	0.21	1.84	16.65
	0.019	6032	0.365	5.5	5.80
	0.019	6513	0.65	17.5	2.05
	0.019	7290	0.98	39.4	1.06
	0.0254	4804	0.41	7.0	4.55
	0.0254	5237	0.78	25.2	1.44
	0.0254	5544	0.98	39.6	1.00
	0.0254	6142	1.3	69.4	0.66
	0.0254	7034	1.63	108.5	0.51
	0.0317	8195	2.28	211.6	0.40
	0.0381	3431	0.48	9.6	2.98
	0.0381	3603	0.57	13.5	2.32
	0.0381	3742	0.72	21.6	1.56
	0.0381	3990	0.88	32.2	1.17
	0.0381	4025	0.95	37.5	1.02
	0.0381	4479	1.16	55.7	0.81
	0.0381	7160	2.25	207.2	0.42
	0.0444	7712	2.52	260.2	0.44
	0.0508	2673	0.305	3.9	6.16
	0.0508	2909	0.58	14.0	2.07
	0.0508	3416	1.21	60.8	0.66
	0.0571	2728	0.51	10.9	2.67
	0.0571	2981	0.81	27.4	1.28
	0.0571	3124	0.94	36.8	1.05

	0.0571	3621	1.25	65.0	0.78
	0.0571	3958	1.47	89.7	0.65
Suspension 2	0.0127	6698	0.395	8.6	3.90
	0.0159	6450	0.73	29.1	1.41
	0.019	7290	1.54	127.8	0.46
	0.0254	6123	1.5	122.3	0.52
	0.0381	2937	0.48	12.8	2.41
	0.0381	3214	0.83	38.0	0.97
	0.0381	3815	1.4	107.6	0.46
	0.0381	4179	1.66	150.8	0.38
	0.0381	7160	2.5	338.9	0.36
	0.0444	7712	2.56	356.6	0.44
	0.0508	2437	0.41	9.3	3.06
	0.0508	2673	0.85	40.0	0.88
	0.0508	4083	1.83	183.8	0.41
	0.0571	2352	0.54	16.2	1.86
	0.0571	2765	1.14	71.8	0.61
	0.0571	4003	2.04	228.5	0.37
Suspension 3	0.0095	6749	0.37	9.4	3.43
	0.0159	6732	1.1	82.1	0.70
	0.019	4199	0.54	20.2	1.76
	0.0254	2795	0.22	3.4	6.93
	0.0254	3179	0.54	20.2	1.51
	0.0254	3704	1.01	70.2	0.57
	0.0254	6123	1.88	239.4	0.35
	0.0317	3005	0.7	34.0	1.04
	0.0317	8195	2.4	389.9	0.39
	0.0381	2786	0.46	14.7	2.57
	0.0444	2295	0.53	19.6	1.48
	0.0444	2987	1.28	113.3	0.45
	0.0508	2183	0.6	25.1	1.19
	0.0508	2493	1.07	79.4	0.52
	0.0508	3002	1.49	153.5	0.39
	0.0508	4000	1.95	261.7	0.37
	0.0571	2229	0.75	39.2	0.93
	0.0571	2706	1.33	122.6	0.46
	0.0095	6751	0.716	45.8	0.98
	0.0159	6432	1.29	148.3	0.50
	0.019	3560	0.65	38.5	0.99
	0.019	4035	0.97	85.1	0.55
	0.019	7290	1.75	271.5	0.39
	0.0254	2711	0.15	2.1	15.39
	0.0254	2779	0.54	26.8	1.25
	0.0254	3210	0.88	70.6	0.62

Suspension 4	0.0254	3649	1.15	120.0	0.46
	0.0317	2865	0.76	53.0	0.87
	0.0381	2702	0.97	86.2	0.58
	0.0444	2415	0.95	82.9	0.57
	0.0508	2222	0.95	83.0	0.54
	0.0571	1910	0.58	31.1	1.09
	0.0571	2098	0.9	74.6	0.60
	0.0571	2595	1.45	192.7	0.38
	0.0571	3707	1.88	322.7	0.42
Suspension 5	0.0095	6751	0.94	115.8	0.61
	0.0127	3332	0.28	10.8	3.27
	0.0159	3150	0.53	38.3	1.07
	0.0159	6432	1.58	327.1	0.35
	0.019	2887	0.67	61.2	0.70
	0.019	3891	1.1	162.6	0.43
	0.019	7290	1.89	468.0	0.35
	0.0254	2018	0.295	12.0	2.17
	0.0254	2394	0.61	51.1	0.79
	0.0254	2544	0.78	83.1	0.55
	0.0254	3041	1.08	158.2	0.41
	0.0254	4604	1.52	310.0	0.40
	0.0254	6123	1.79	427.2	0.42
	0.0317	2420	0.94	120.8	0.44
	0.0381	2309	0.95	123.8	0.47
	0.0381	7160	2.52	848.9	0.39
	0.0571	1711	0.69	65.8	0.60
	0.0571	2204	1.22	204.5	0.40
	0.0571	2801	1.57	337.5	0.40
Suspension 6	0.0095	6751	1.26	402.6	0.37
	0.0127	3319	0.76	156.5	0.51
	0.0127	6693	1.4	507.1	0.40
	0.0159	2984	0.86	201.5	0.42
	0.0159	6432	1.54	621.1	0.39
	0.019	2516	0.82	185.2	0.41
	0.019	3838	1.26	427.7	0.35
	0.019	6032	1.64	711.2	0.38
	0.019	7290	1.9	942.7	0.36
	0.0254	1708	0.42	49.8	0.79
	0.0254	2009	0.71	140.9	0.45
	0.0254	3006	1.18	382.2	0.37
	0.0254	4102	1.49	602.4	0.37
	0.0254	6023	1.92	984.5	0.38
	0.0381	2000	0.77	166.9	0.59
	0.0381	2310	1.02	291.1	0.46

	0.0381	5932	2.31	1445.2	0.38
	0.0444	2003	0.93	243.3	0.47
	0.0571	1314	0.17	8.3	2.95
	0.0571	1481	0.63	112.8	0.49
	0.0571	2007	0.98	271.2	0.56
	0.0571	2832	1.51	638.1	0.47
	0.0571	3879	1.89	993.2	0.49
	0.0571	6002	2.8	2146.8	0.40

Fig. 8 illustrates the numerical model to simulate the settlement of spheres in the clay suspensions built with EDEM. The geometry of the numerical model is the same as the physical model shown in Fig. 7. The physical parameters for the numerical model can be found in Tables 2 and 3.

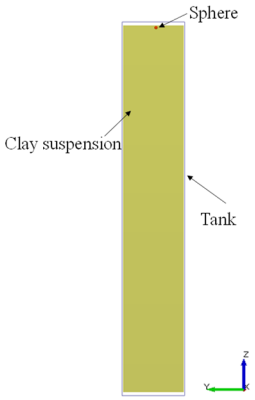

Fig. 8 Numerical model for reproducing the settling of spheres in the clay suspensions built with EDEM

Once again, sensitivity analysis is necessary to determine the optimal time step. Fig. 9 shows the variation of the terminal velocity v_{ter} of spheres as a function of time step. It is seen that the numerical results become stable once the time step is equal to or smaller than 1×10^{-1} s for spheres with four different diameters. Further reductions of time step do not significantly change the simulation results.

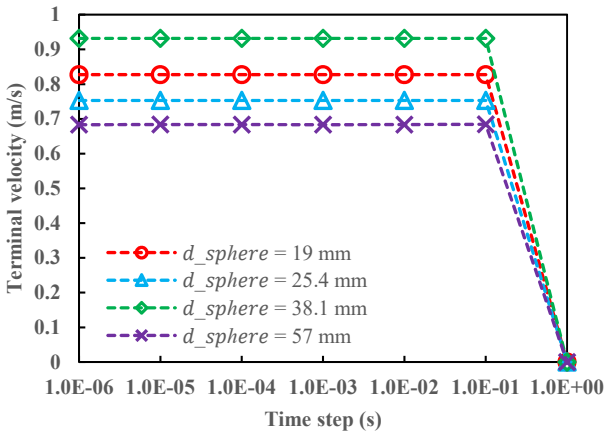

295

296 **Fig. 9** The variation of terminal settling velocity v_{ter} of spheres as a function of time step

297 Fig.10 illustrates the variation of the settling velocity of spheres at t = 0.01 s as a function of time
298 step. The numerical results become stable when the time step is reduced to 1×10^{-4} s, a value much
299 smaller than the optimal time step of 1×10^{-1} s for simulating the terminal velocity. This is because
300 the settling velocity changes rapidly with time at the beginning and tends to become constant when
301 it is close to the terminal velocity. The time step should be small enough to capture the rapid
302 change of velocity with time at the beginning of settlement. When the velocity is close to the
303 terminal velocity, the velocity changes with time becomes small and a large time step can become
304 enough to capture the velocity change with time. To ensure the numerical results are stable for the
305 spheres at all different times, the optimal time step is determined as 1×10^{-5} s.

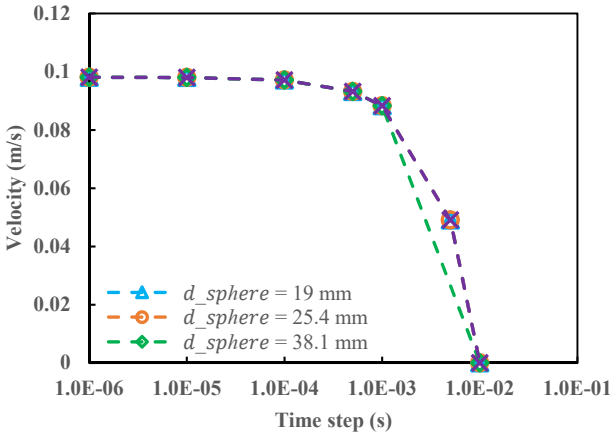

306

307 **Fig. 10** The variation of settling velocity of spheres (t = 0.01 s) as a function of time step

308 Fig. 11 presents the variation of the terminal velocities of spheres as a function of sphere density
309 for different diameters of spheres settling in clay suspensions 1 to 6 (Fig. 11a to 11f), obtained by

laboratory tests and f-EDEM model by considering the optimal time step of 1×10^{-5} s. One sees that the agreements between the experimental results and numerical predictions are very good for all the spheres in different clay suspensions. These results confirm that the f-EDEM model can be applied (i.e. is applicable or has the required power) to simulate the settlements of spheres in clay suspensions.

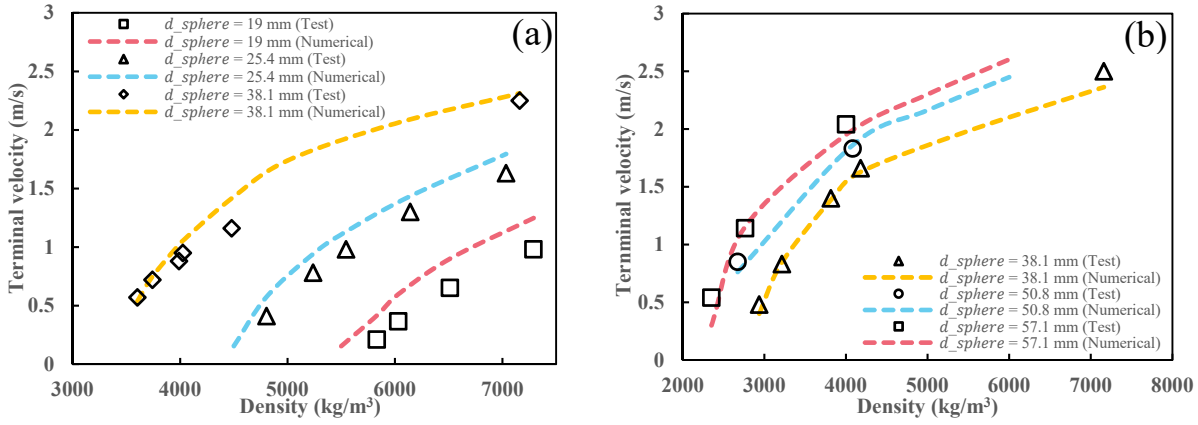

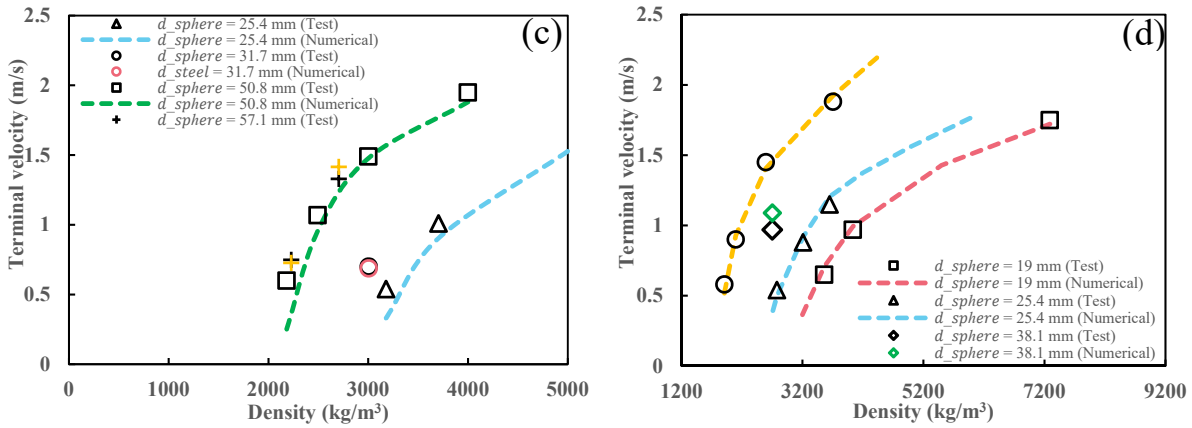

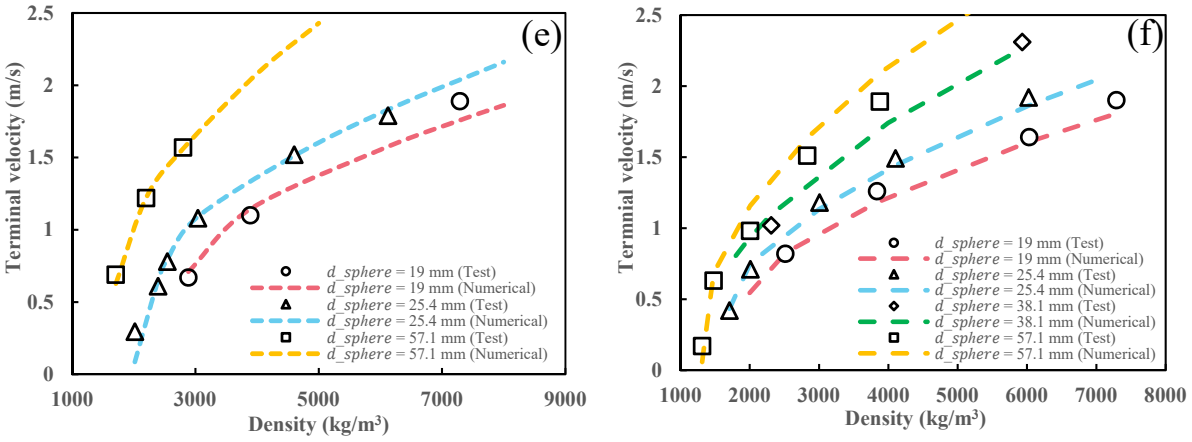

Fig. 11 Variation of the terminal velocities of spheres as a function of sphere density for different diameters of spheres settling in clay suspensions 1 to 6, obtained by the test and f-EDEM model with the optimal time step of 1×10^{-5} s: (a) suspension 1; (b) suspension 2; (c) suspension 3; (d) suspension 4; (e) suspension 5; (f) suspension 6

4.2. Application of the f-EDEM model to numerically reproduce tests of steel balls falling into a paste backfill

To further exam the applicability of f-EDEM model to simulate the settlement of particles in other non-Newtonian fluids, a series of particle settlement tests have been realized in the laboratory with steel balls and a paste backfill, which is usually characterized as a Bingham plastic fluid (Potvin et al., 2005). The number of calibration parameters is minimized through the measurements as long as possible of the material parameters of the tested steel balls and paste backfill. Typical values are taken from the literature for the Young's modulus and Poisson's ratio of steel balls as well as the rolling resistance coefficient of steel ball of 12.6 in diameter. This results in Table 4, by which one sees that the calibration is necessary only on the plastic viscosity of the tested paste backfill. The yield stress of the tested paste backfill was obtained through slump tests (see details given Appendix I), whereas the restitution coefficient between the steel balls was measured by conducting steel ball drop tests (see details given Appendix II) and the static friction coefficient between the steel balls was measured through tilt tests with a steel block and a steel plate (see details given in Appendix III).

Table 4 Physical parameters for the tests of steel ball falling into a paste backfill

Steel ball parameters	Diameter, d_{steel} (mm)	8, 12.6, 16	Measured
	Density, ρ_{steel} (kg/m^3)	8135	Measured
	Falling height, H_f (mm)	0, 105, 150, 255, 405, 555	Measured
	Young's modulus, E (GPa)	200	Marinack et al., 2013
	Poisson's ratio, ν	0.3	Marinack et al., 2013
Paste backfill parameters	Solids content, P (%)	75	Measured
	Yield stress, τ_y (Pa)	136	Measured
	Viscosity, η_B (Pa.s)	0.7	Calibrated
	Restitution coefficient, μ_e	0.612	Measured

Interaction parameters between steel ball of 12.6 mm in diameter	Static friction coefficient, μ_s	0.341	Measured
	Rolling resistance coefficient, μ_r	0.002	Minkin & Sikes, 2018

Fig. 12 presents a schematic presentation and a picture of the physical model used to test the penetration of a single steel ball in the tested paste backfill (see details given in Zhang & Li, 2023 for the preparation of the paste backfill). The prepared paste backfill was poured into a cylinder of 75 mm in diamter and 150 mm high, quickly followed by the release of a steel ball at a predetermined falling height H_f. Three steel balls were used in the tests with each having a diameter of 8, 12.6, or 16 mm, respectively. Each steel ball was dropped into the paste backfill from six different falling heights (see Table 4). Once the steel ball falled into the paste backfill, the mold was fixed on the table and remained untouched until the paste backfill became hard enough for cut. During the waiting time, any movements or vibrations, which are subjetive to affect the physical model, were not allowed.

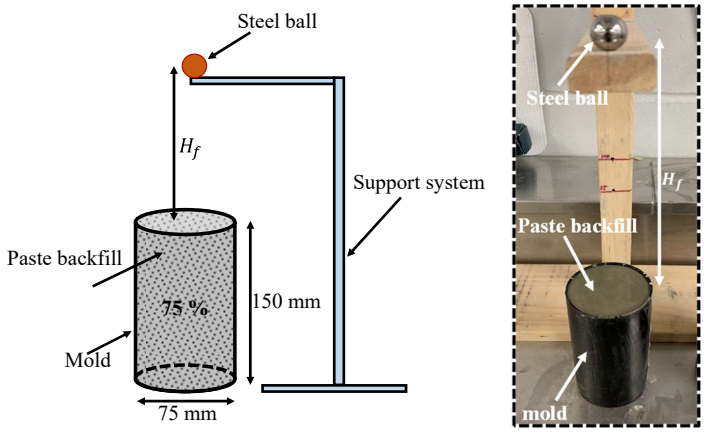

(a) (b)

Fig. 12 Tests of a steel ball falling into a paste backfill: (a) schematic presentation; (b) physical model

Figure 13 shows a typical specimen (Fig. 13a) of hardended paste backfill taken out from the mold and and the steel ball of 16 mm in diameter (Fig. 13b) exposed after gently cut of the paste backfill. The settling distance of the steel ball within the paste backfill was measured using an electronic

digital caliper (Fig. 13b). The procedure was repteated for different steel balls and different predetermined falling heights.

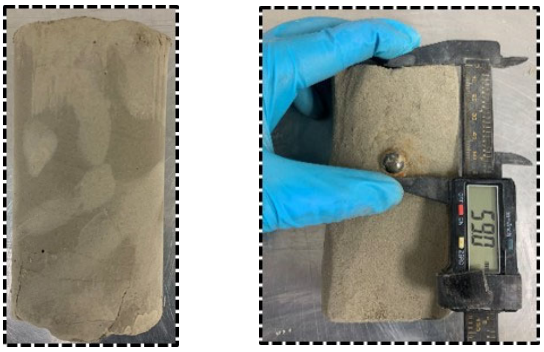

(a) (b)

Fig.13 Measurement of settling distance of a steel ball within the paste backfill: (a) hardened paste backfill sample taken out from the mold; (b) measuring the settling distance of steel ball within the paste backfill

Fig. 14 presents a numerical model of the physical model presented in Figure 12 built with EDEM. The physical parameters can be found in Table 4, expect the viscosity of the paste backfill, which needs to be obtained by numerical calibration against the experiment results. Sensitivity analyses of time step presented in Fig. 15 indicate that the optimal time step for all the three steel balls is around 1×10^{-5} s. A value of 5×10^{-6} s was retained for being more conservative.

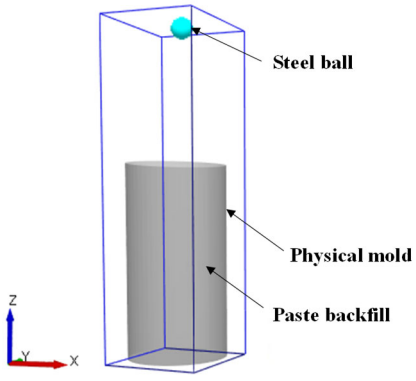

Fig. 14 Numerical model of the physical model presented in Fig. 12 for reproducing the settlement of a single steel ball within the paste backfill built with EDEM

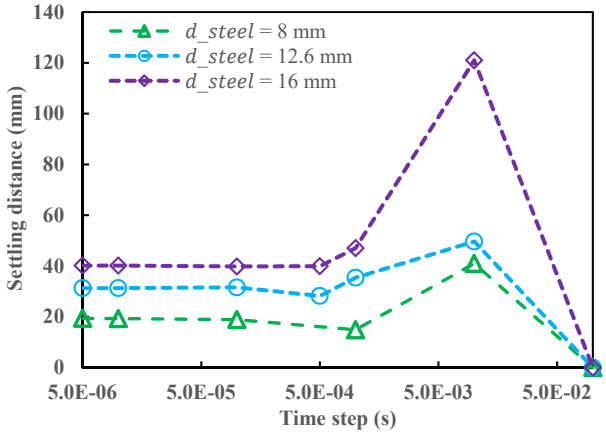

370

371 **Fig. 15** The variation of settling distance of steel balls as a function of time step

372 To calibrate the viscosity of the paste backfill, the test results obtained by using the steel ball of
373 12.6 mm in diameter dropped into paste backfill at a falling height of 255 mm will be reproduced
374 by f-EDEM model. This leads to a viscosity 0.7 Pa.s by which the best agreement between the
375 experimental and numerical results is achieved. This viscosity of paste backfill is then used to
376 predict the other test results obtained with the same steel ball dropped at different falling heights
377 and those obtained with the two other steel balls dropped at different failling heights.

378 Fig. 16 shows the variation of the settling distance of a steel ball in the paste backfill as a function
379 of falling height, obtained by laboratory results and calculated by f-EDEM model by using the
380 physical parameters shown in Table 4 along with the calibrated viscosity of 0.7 Pa.s for the paste
381 backfill. It can be seen that the agreement between the numerical and experimental results for the
382 case of steel ball of 12.6 mm dropped at a falling height of 255 mm is almost perfect because these
383 tests results were used to calibrate the viscosity of the paste backfill. For the tests with the same
384 steel ball dropped at different heights and for tests with the other two steel balls (8 and 16 mm in
385 diameter, respectively) dropped at different falling heights, the agreements between the
386 experimental results and those predicted by using the calibrated f-EDEM model remain quite good,
387 except for the settlement of the steel ball of 16 mm in diameter dropped at falling heights of 105
388 and 150 mm, respectively. In general, the agreements between the experimental results and
389 numerical results predicted by applying the f-EDEM model are good. The f-EDEM model can thus
390 be considered as capable of simulating the settlement of a single steel ball in the paste backfill.

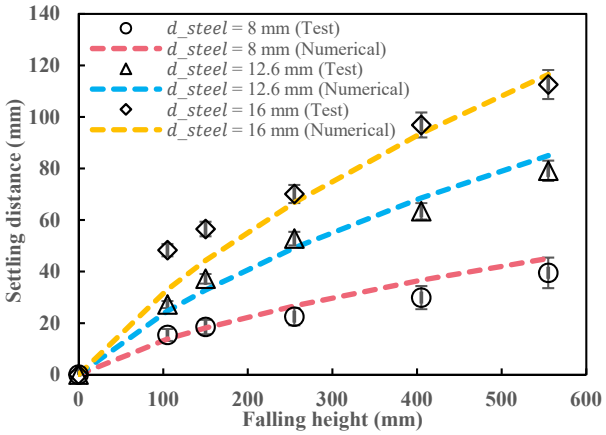

391

392 **Fig. 16** Variation of settling distance of steel balls as a function of falling height, obtained by test and f-
393 EDEM model with optimal time step of 5×10^{-6} s

394 To further show the applicability of the f-EDEM model, additional falling tests have been
395 performed with 68 steel balls having a diameter of 12.6 mm initially held in a funnel, dropped at
396 a falling height of 15 cm into the same paste backfill as that one used for falling tests with a single
397 steel ball (see details given in Table 4). Fig. 17 shows a schematic presentation (Fig. 17a) and a
398 picture (Fig. 17b) of the physical model.

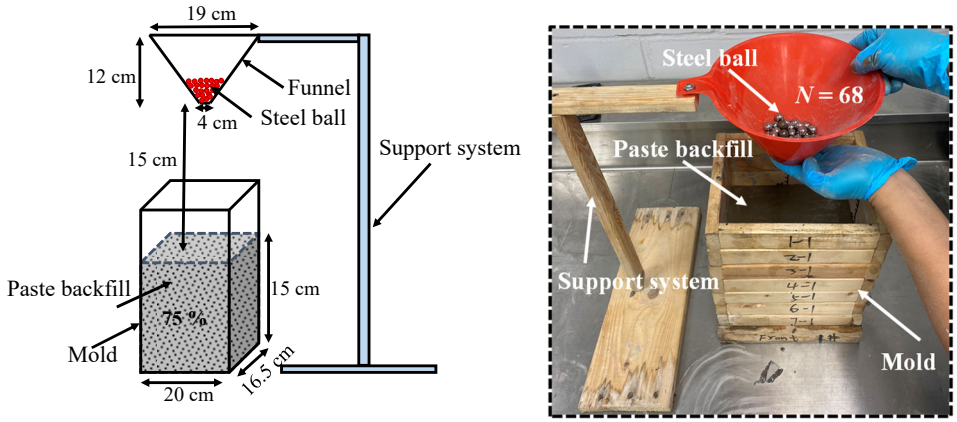

399

400 (a) (b)

401 **Fig. 17** Physical model used for the falling tests with 68 steel balls of 12.6 mm in diameter, initially held
402 in a funnel and dropped into the paste backfill at a falling height of 15 cm: (a) schematic presentation; (b)
403 a picture

404 Once again, the mold was left untouched on the table for a couple of weeks after having poured
405 the steel balls into the paste backfill. During the waiting time, no vibrations and movements were

allowed. When the paste backfill became hard enough, the mold was removed and the hardened paste backfill was gently cut layer by layer to obtain the spatial position in terms of X, Y and Z coordinates of each steel ball, as shown in Fig. 18.

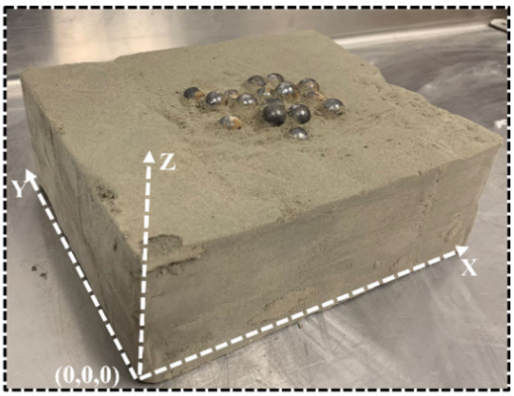

Fig. 18 Identifying the spatial distributions of steel balls in the paste backfill

Fig. 19 presents the numerical model of Fig. 17, built with EDEM. It is worth mentioning that all the required parameters for the numerical model have been determined as shown in Table 4 with the viscosity of 0.7 Pa.s for the paste backfill obtained by calibration process against the experimental results of falling tests with a single steel ball of 12.6 mm dropped at a falling height of 255 mm. Subsequently, all the numerical results presented hereafter are numerical predictions.

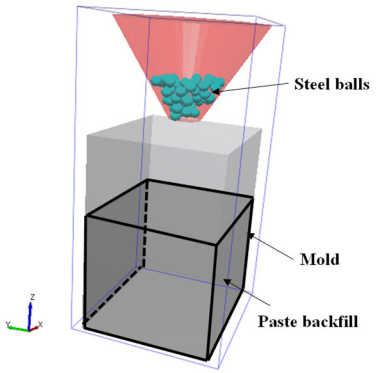

Fig. 19 Numerical model for reproducing the test of multiple steel balls falling into a paste backfill

Fig. 20 illustrates the variation of steel ball number, N, at t = 0.5 s as a function of time step ΔT. One sees that only one steel ball was generated when the time step is 2.43 $\times 10^{-5}$ s. The number of steel ball N = 4 when the time step decreases to 2.08 $\times 10^{-5}$ s. Once the time step is reduced to 1.04 $\times 10^{-5}$ s or smaller, the number of steel ball becomes stable (N = 68). The optimal time step is thus

taken as 1.04×10^{-5} s. This value is larger than 20% T_R (1.39×10^{-6} s), a value recommended by most DEM simulations. The results once again confirm that sensitivity of time step is always necessary to conduct case by case to find the optimal time step in order to ensure stable and reliable numerical result with the shortest time of calculations.

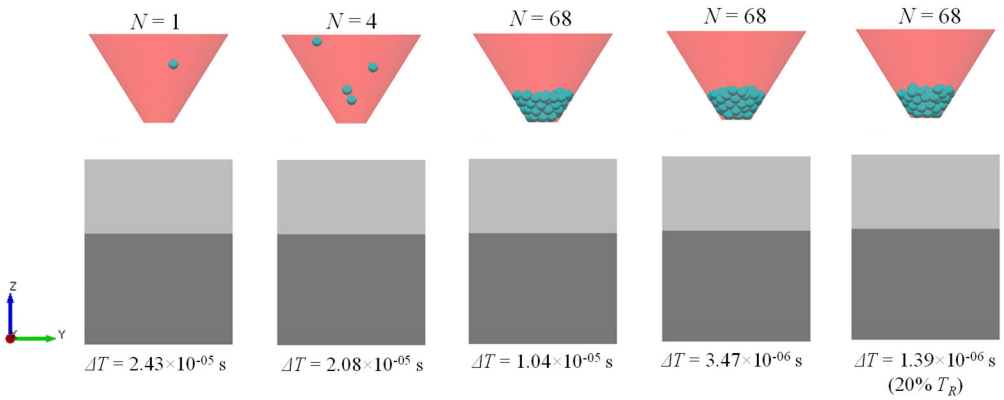

Fig. 20 Variation of steel ball number N at t = 0.5 s with the change of time step ΔT

Fig. 21 presents the distributions of steel balls in the vertical direction (along Z axis) in the paste backfill, obtained by laboratory tests (Fig. 21a, plotted by inputting the measured coordinates X, Y and Z of each sphere in Python) and predicted by f-EDEM model with the optimal time step of 1.04×10^{-5} s (Fig. 21b). Both the experimental and numerical results indicate that all the steel balls remain in suspending within the paste backfill along the vertical heights from Z = 8.5 to 13.5 cm. The only way to explain this phenomenon is to attribute it to the loss of kinematic energy of steel balls because of the large drag force provided by the paste backfill with high viscosity and yield stress. The steel balls quickly experience deceleration as soon as they penetrate into paste backfill. They can stop moving and remain in suspending probably because the mass of the steel ball is not large enough to overcome the drag force in the paste backfill when the settling velocity falls to zero. Moreover, some steel balls can penetrate deeper in the paste backfill due to the hit and impact of upper steel balls fallen later. In general, a good agreement between the experimental and numerical results is obtained, as shown by Figs. 21a and 21b.

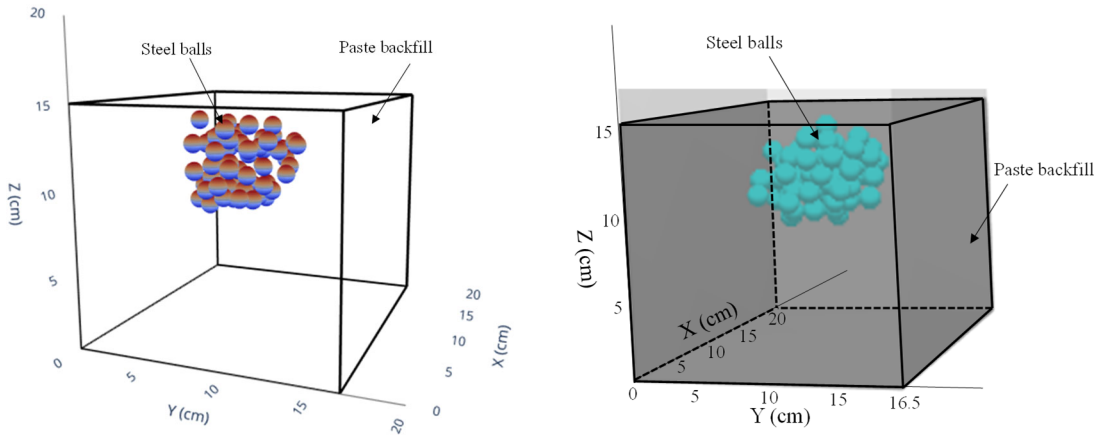

(a) (b)

Fig. 21 Distributions of steel balls in the vertical direction (along *Z* axis) in the paste backfill, obtained by laboratory tests and predicted by f-EDEM model with the optimal time step of 1.04×10^{-5} s: (a) test results; (b) numerical results

To further evaluate the quality of agreement between the experimental and numerical modeling with the f-EDEM model, the horizontal distributions of the steel balls at different vertical heights are also examined. Fig. 22 shows the distributions of steel balls at a horizontal plane varying from Z = 13.5 to 8.5 cm (Figs. 22a to 22f), obtained by the laboratory tests and predicted by the numerical modeling with the f-EDEM model. It should be noted that the numerical results are presented in terms of probability. This is because it is very difficult, if not impossible, to reproduce exactly the initial spatial position of each individual particle. The initial spatial position of each individual particle remains undefined in the laboratory tests, while the individual particles are randomly generated by the f-EDEM model. These differences in initial spatial positions of particles can result different collisions during their movements. The settlements and spatial distributions can thus be different from one simulation to another. To reduce the uncertainty associated with the initial generation of particles, the simulations were repeated 15 times. The number of presence of particle in each cluster was then counted, resulting in the presence probability of a particle, as shown in Figs. 22a to 22f.

All the numerical results indicate that the steel balls are highly probable to be present in the small center area while the probability of presence reduces to 40% or less along the perimeter of the center area. The high probabilities in the center area are confirmed by the experimental results. Along the perimeters of center area, the observed presence of particles cannot confirm or disaffirm

464 the numerical results with a probability of 40%. However, the agreements between the numerical
465 and experimental results are quite good in term of the perimeter positions for all the planes varying
466 from Z = 12.5 to 9.5 cm, except in the plane of Z = 8.5 cm, in which the positions of perimeter
467 particles are slightly different from those predicted by the numerical modeling (Fig. 22f). In
468 general, the agreements between the experimental results and numerical predictions are quite good,
469 considering numerous uncertainties in the laboratory tests. The ability and applicability of the f-
470 EDEM model in simulating the settlement of multiple steel balls in paste backfill are also
471 confirmed.

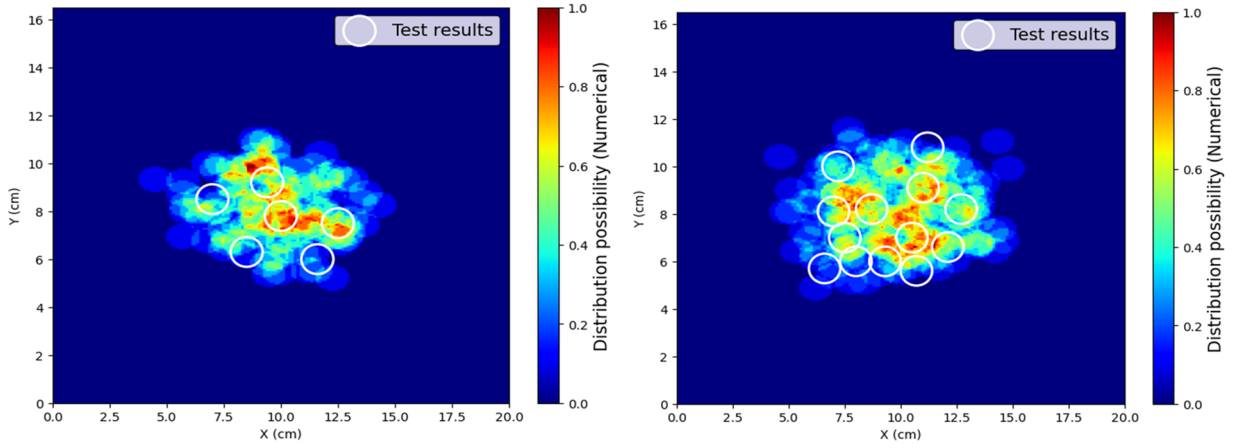

472

473 (a) (b)

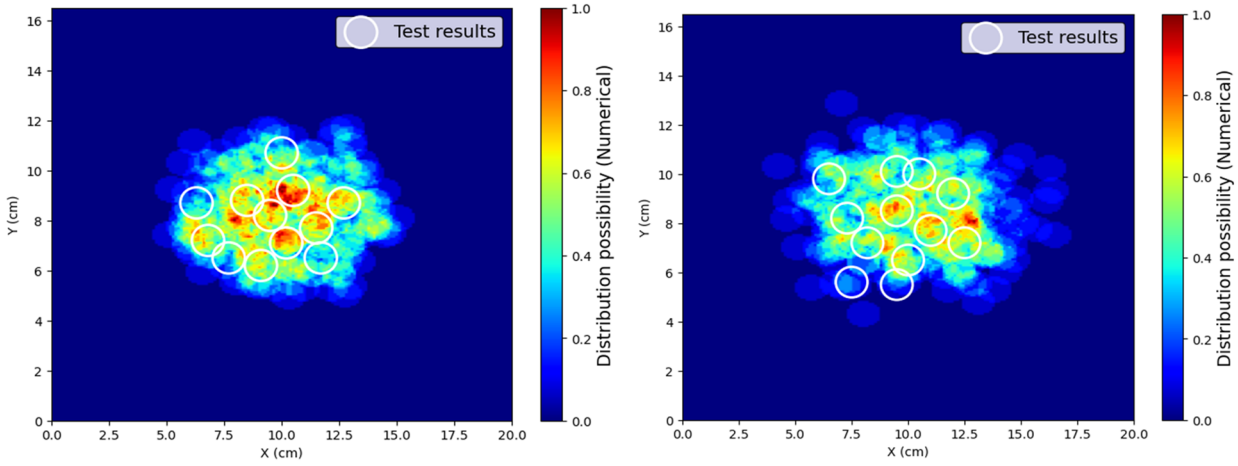

474

475 (c) (b)

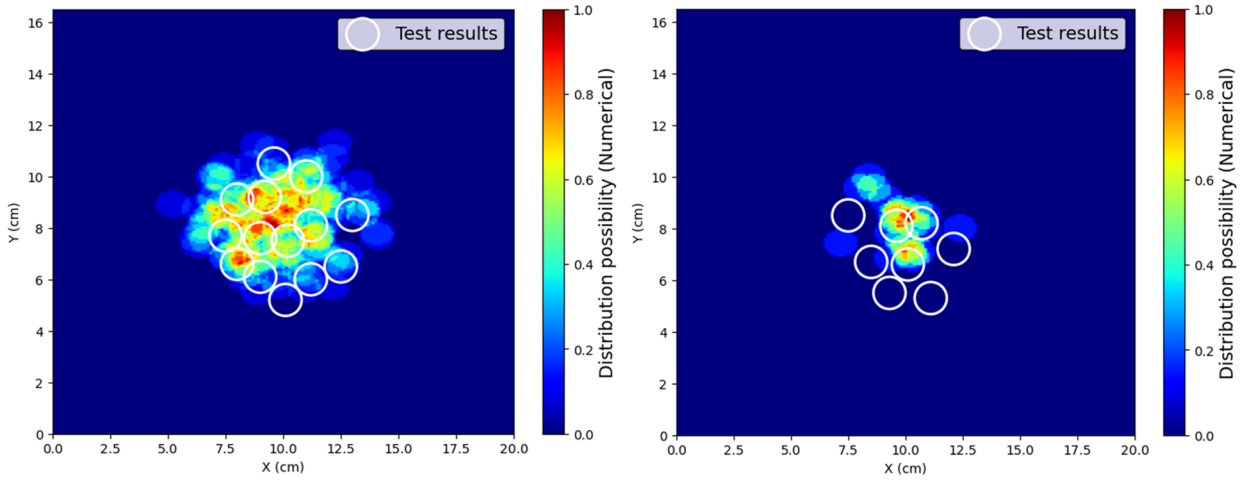

(e) (f)

Fig. 22 The distributions of steel balls at a horizontal plane varying from Z = 13.5 to 8.5 cm, obtained by the laboratory tests and predicted by the f-EDEM model: (a) Z = 13.5 cm; (b) Z = 12.5 cm; (c) Z = 11.5 cm; (d) Z = 10.5 cm; (e) Z = 9.5 cm; (f) Z = 8.5 cm

5. Discussion

In this study, the formulation and implementation of fluid forces have been realized in the EDEM code via a user-defined-force-model to simulate the settlement of spherical particles in different fluids. This results in a new model, called f-EDEM model. The f-EDEM model has been validated against an analytical solution while its ability and applicability have been confirmed through the numerical reproductions of several experimental results. It can thus be used to solve several engineering problems associated with the settlement of particles in fluids. However, one needs to keep in mind that this study involves several limitations.

In this study, the fluids (e.g., clay suspension and paste backfill) were represented by the buoyance and drag forces. The numerical model does not correspond to the real situation with the physical presence of the simulated fluid. In the simulation, the flow velocity of the fluid is set to be always zero (fluid at rest). The slip velocity between the particle and fluid thus be considered equals the settling velocity of particle. However, the model is not able to take into account the effects of particle movement on the motion of fluid (e.g., the splash of fluid after the particle is dropped) because the flow of fluid cannot be described in the simulation. In this situation, the accuracy of slip velocity between the particle and fluid can be influenced. For the cases with even more complicated interactions, such as two-way simulations (the fluid flow affects the particles

movement and the particles in turn affect the motion of fluid) or the particle-related inner stream flow (fluid flow between the particles), the coupling with CFD solver will be necessary as these simulations requires the Navier-Stokes equation to describe the flow of the fluids. More work is thus needed to render the model able to simulate these complicated cases in our future study. In addition, the sedimentation or consolidation of clay suspensions and paste backfill cannot be taken into account using the proposed model.

By comparing the numerical and the test results, the applicable particle density obtained by this study ranges from 1314 to 8135 kg/m^3 and the particle diameter ranges from 8 to 57.1 mm. Particles out of these specific ranges will need to be examined by conducting more numerical simulations and lab tests.

The ability of f-EDEM model to simulate the settlement of particles in part of Bingham plastic fluids (e.g., clay suspensions and paste backfill) has been confirmed by reproducing and predicting the experimental results. However, the drag force model is not a generalized model for simulating the settlement of particles in all non-Newtonian fluids. The applicability of f-EDEM model to simulate the settling of particles in other Bingham plastic fluids remains to be examined by comparing the numerical results with more physical test results. In addition, the proposed drag model is developed for particles with spherical shapes. For simulations using spheres to represent non-spherical particles (e.g., rock particles), one needs to make sure that the shape-related effects can be neglected due to the relatively small errors coming from the particle-shape-approximation (as spheres) and have insignificant influences on the overall simulation results. Otherwise, the shape effects will need to be addressed and considered by changing some other parameters. This will be part of our future works and publications.

Another limitation of the f-EDEM model is related to the consideration of fully submerged particles. This can be considered reasonable with small particles. When the dropped particles are large, the changes of submergence of the particle from the moment of contact with the top surface of the fluid to fully submerged state cannot be captured by the f-EDEM model. More work is thus necessary to take into account this aspect in the future.

6. Conclusions

In this study, fluid forces have been formulated and directly implemented in EDEM code, resulting in a new model, named f-EDEM. Using this model, the settlement of particles in fluids can be simulated by a single DEM code without the need of coupling with a CFD or SPH solver. The good agreement between the analytical solution and numerical results of the settling velocity of a particle in water indicates that the f-EDEM model was successfully validated. Further comparisons and good agreements between the experiment results and numerical reproduction of spheres settling in clay suspensions and steel balls settling in paste backfill indicate that the f-EDEM model is applicable and has the ability of simulating the settlements of particles in Newtonian and some Bingham plastic fluids. In addition, this study shows that the time step recommended by the manual of most DEM codes (10 to 20% of Rayleigh time) can be excessively small, leading to a high computational cost. It is always necessary to conduct sensitivity analysis of time step, case by case, to find the optimal time step in order to ensure stable and reliable numerical result with the shortest time of calculations.

Acknowledgements

The authors acknowledge the financial support from the Natural Sciences and Engineering Research Council of Canada (NSERC RGPIN-2018-06902), Natural Sciences and Engineering Research Council of Canada (NSERC ALLRP 580767 - 22), Fonds de recherche du Québec – Nature et technologies (FRQNT 2017-MI-202860), and industrial partners of the Research Institute on Mines and the Environment (RIME UQAT – Polytechnique; http://rime-irme.ca).

Appendix I: Measurement of yield stress of paste backfill by slump tests

Slump tests were conducted to measure the yield stress of paste backfill using the method proposed by Pashias and Boger (1996). The test procedures are presented in Fig. A1. A cylinder model was chosen for the tests because this geometry is considered as the most accurate model to predict the yield stress of mine backfill based on the study of Clayton et al. (2003). The cylinder model is made of Polyvinyl chloride and has an inner diameter of 152 mm and a height of 152 mm (Fig. A1a). In the tests, the paste backfill with solids content by mass of 75% was first poured into the cylinder mold. The mold was then gently lifted in a vertical direction. The slump height S of paste

backfill was measured using a ruler (Fig. A1b). The tests were repeated three times to minimize the test errors.

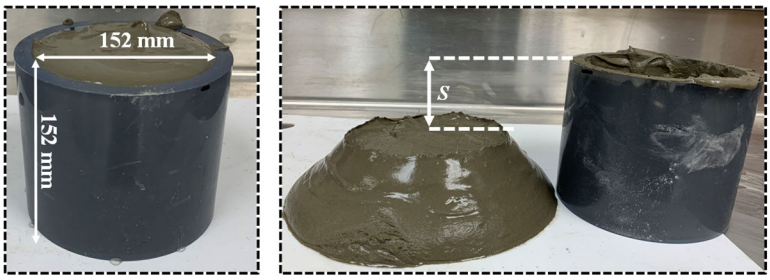

(a) (b)

Fig. A1 Slump tests: (a) cylinder mold filled with paste backfill; (b) measure the slump height

The yield stress of paste backfill is then calculated based on the cylinder model theory given by Pashias and Boger (1996). First, a relationship between the dimensionless slump height and dimensionless yield stress can be expressed as:

$$S' = 1 - 2\tau_y'\left[1 - \ln 2\tau_y'\right] \tag{A1}$$

where S' is the dimensionless slump height, τ_y' is the dimensionless yield stress.

The dimensionless variables can be expressed as:

$$S' = S/H \tag{A2}$$

where S is the slump height, H is the height of cylinder model.

$$\tau_y' = \tau_y/\rho_{\_paste}gH \tag{A3}$$

where τ_y is the yield stress, $\rho_{\_paste}$ is the density of paste backfill.

Based on equations (A1) to (A3), the yield stress τ_y of paste backfill can be calculated. Table A1 presents the test parameters and calculated yield stress of paste backfill.

Table A1 Slump test results

Model height, H (mm)	Model inner diameter, D (mm)	Paste backfill density, $\rho_{\_paste}$ (kg/m^3)	Slump height, S (mm)	Yield stress, τ_y (Pa)	Average yield stress (Pa)
152	152	1843	102	135	

152	152	1843	103	131	136
152	152	1843	100	143	

Appendix II: Determination of restitution coefficient between steel balls through steel ball drop tests

The restitution coefficient between steel balls were determined by conducting the tests of a steel ball re-bounce in a steel plate (Fig. A2). In the tests, a steel ball with diameter $d_{\_steel}$ = 8 mm was drop into a steel plate at a pre-determined falling height H_f. The re-bounce height H_r of steel ball in the plate was recorded using a high-speed camera. The steel ball was dropped at five different falling heights with each test was repeated five times to minimize the test errors.

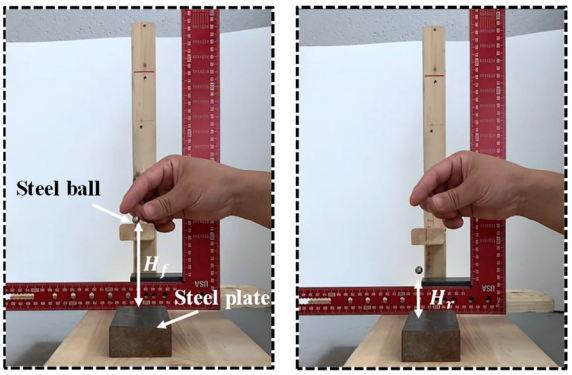

(a) (b)

Fig. A2 Steel ball drop tests: (a): drop the steel ball at falling height of H_f (b): measure the re-bounce height H_r of steel ball

The restitution coefficient μ_e is then calculated by Sandeep et al. (2021):

$$\mu_e = \sqrt{\frac{H_r}{H_f}} \tag{A4}$$

The physical parameters and test results are presented in Table A2.

Table A2 Physical parameters and results of a steel ball re-bounce tests

Steel ball diameter $d_{\_steel}$ (mm)	Steel ball density $\rho_{\_steel}$ (kg/m^3)	Steel ball falling height H_f (mm)	Steel ball re-bounce height H_r (mm)	Restitution coefficient μ_e	Average
8	8135	95	37.0	0.624	0.612
		188	72.0	0.619	
		252	90.9	0.601	
		318	118.0	0.609	
		398	146.9	0.608	

583

584 A numerical model (Fig. A3) was constructed to reproduce the test results by using the average
585 restitution coefficient (μ_e = 0.612). The input physical parameters of the numerical model can be
586 found in Table A2.

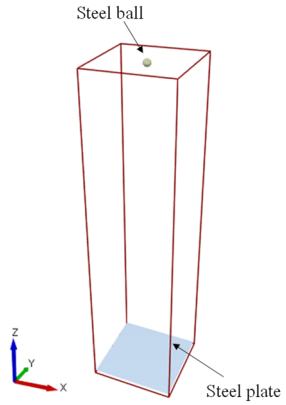

587

588 **Fig. A3** Numerical model for reproducing the test of steel ball drop in a steel plate

589 Fig. A4 presents the comparisons between the test results and numerical results of re-bounce height
590 of steel ball at different falling heights. It is seen that the numerical results match perfectly with
591 the test results at each falling height. The results confirm that the numerical model can precisely
592 predict the re-bounce height of steel ball at different falling heights by using the measured
593 restitution coefficient.

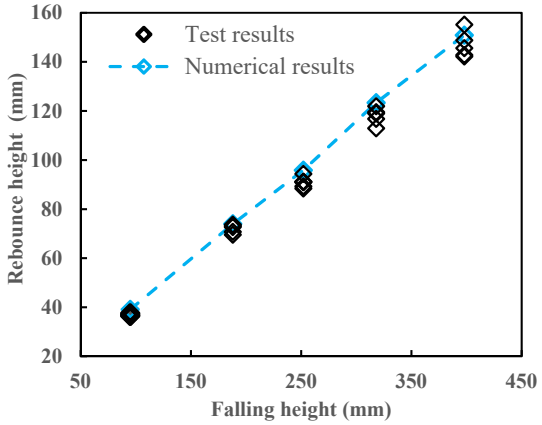

Fig. A4 Variation of re-bounce height of steel with the falling height, obtained by test results and numerical results

Appendix III: Determination of the static friction coefficient between steel balls through tilt tests

The static friction between the steels were estimated by conducting the tilt test with a steel block and a steel plate (Fig. A5). In the test, the steel plate was slightly lifted to a height H_l at where the steel block started to move. The lift height H_l was then recorded. The test was repeated five times to reduce the measurement error.

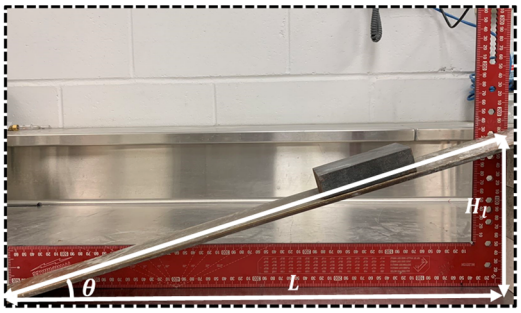

Fig. A5 The tilt test with a steel block and a steel plate

The static friction coefficient is calculated by (Ibrahim Dickey et al., 2011):

$$\mu_s = \frac{H_l}{L}$$

where μ_s is the static friction coefficient, H_l is the lift height, L is distance between the vertex at the angle θ and the vertex at the vertical angle.

609 The detailed test results are presented in Table A3.

610 **Table A3** Test results of a steel block slide on a steel plate

Trials	L (cm)	H_l (cm)	μ_s	Average
1	600	205	0.342	
2	600	205	0.342	
3	600	202	0.337	0.341
4	600	202	0.337	
5	600	208	0.347	

611 # References

612 Blackery, J., & Mitsoulis, E. (1997). Creeping motion of a sphere in tubes filled with a Bingham plastic
613 material. *Journal of Non-Newtonian Fluid Mechanics, 70*(1), 59-77.
614 https://doi.org/https://doi.org/10.1016/S0377-0257(96)01536-4

615 Bokharaeian, M., Naderi, R., & Csámer, Á. (2021). Numerical experimental comparison of mudflow by
616 smoothed particle hydrodynamics (SPH). *International Review of Applied Sciences and*
617 *Engineering, 13*(1), 22-28. https://doi.org/10.1556/1848.2021.00263

618 Burns, S. J., Piiroinen, P. T., & Hanley, K. J. (2019). Critical time step for DEM simulations of dynamic
619 systems using a Hertzian contact model. *International Journal for Numerical Methods in*
620 *Engineering, 119*(5), 432-451. https://doi.org/10.1002/nme.6056

621 Capozzi, L. C., Barresi, A. A., & Pisano, R. (2019). Supporting data and methods for the multi-scale
622 modelling of freeze-drying of microparticles in packed-beds. *Data Brief, 22*, 722-755.
623 https://doi.org/10.1016/j.dib.2018.12.061

624 Casarin, J., Franco, A., Germer, E., & Pivovarski, R. (2022). Numerical simulation of the particle settling
625 in a Bingham fluid using the two-way coupling CFD-DEM scheme. *Journal of Theoretical and*
626 *Applied Mechanics*, 409-422. https://doi.org/10.15632/jtam-pl/150239

627 Chhabra, R. (2006). Bubbles, drops, and particles in non-Newtonian fluids.
628 https://doi.org/10.1201/9781420015386

629 Clayton, S., Grice, T. G., & Boger, D. V. (2003). Analysis of the slump test for on-site yield stress
630 measurement of mineral suspensions. *International Journal of Mineral Processing, 70*(1-4), 3-21.
631 https://doi.org/10.1016/s0301-7516(02)00148-5

632 Cleary, P. W. (2015). Prediction of coupled particle and fluid flows using DEM and SPH. *Minerals*
633 *Engineering, 73*, 85-99. https://doi.org/10.1016/j.mineng.2014.09.005

634 Cleary, P. W., & Prakash, M. (2004). Discrete-element modelling and smoothed particle hydrodynamics:
635 potential in the environmental sciences. *Philos Trans A Math Phys Eng Sci, 362*(1822), 2003-2030.
636 https://doi.org/10.1098/rsta.2004.1428

637 Cleary, P. W., Sinnott, M., & Morrison, R. (2006). Prediction of slurry transport in SAG mills using SPH
638 fluid flow in a dynamic DEM based porous media. *Minerals Engineering, 19*(15), 1517-1527.
639 https://doi.org/10.1016/j.mineng.2006.08.018

Concha Arcil, F. (2009). Settling velocities of particulate systems. *KONA Powder and Particle Journal, 27*, 18-37. https://doi.org/10.14356/kona.2009006

Cundall, P. A., & Strack, O. D. L. (1979). A discrete numerical model for granular assemblies. *Géotechnique, 29*(1), 47-65. https://doi.org/10.1680/geot.1979.29.1.47

Dedegil, M. Y. (1987). Drag coefficient and settling velocity of particles in non-Newtonian suspensions. *Journal of Fluids Engineering, 109*(3), 319-323. https://doi.org/10.1115/1.3242667

Dhaouadi, W., Marteau, E., Kolvenbach, H., Choukroun, M., Molaro, J. L., Hodyss, R., & Schulson, E. M. (2021). Discrete element modeling of planetary ice analogs: mechanical behavior upon sintering. *Granular Matter, 24*(1). https://doi.org/10.1007/s10035-021-01167-6

Di Felice, R. (1994). The voidage function for fluid-particle interaction systems. *International Journal of Multiphase Flow, 20*(1), 153-159. https://doi.org/https://doi.org/10.1016/0301-9322(94)90011-6

Domínguez, J., Fourtakas, G., Altomare, C., Canelas, R., Tafuni, A., García Feal, O., Martínez-Estévez, I., Mokos, A., Vacondio, R., Crespo, A., Rogers, B., Stansby, P., & Gesteira, M. (2021). State-of-the-art SPH solver DualSPHysics: from fluid dynamics to multiphysics problems.

Ferreira, V. O., Geitani, T. E., Silva, D., Blais, B., & Lopes, G. C. (2023). In-depth validation of unresolved CFD-DEM simulations of liquid fluidized beds. *Powder Technology, 426*. https://doi.org/10.1016/j.powtec.2023.118652

Fonceca Junior, J., Maza, D., & Hidalgo, R. (2021). Modeling particle-fluid interaction in a coupled CFD-DEM framework. *EPJ Web of Conferences, 249*, 09004. https://doi.org/10.1051/epjconf/202124909004

Gingold, R. A., & Monaghan, J. J. (1977). Smoothed particle hydrodynamics: theory and application to non-spherical stars. *Monthly Notices of the Royal Astronomical Society, 181*(3), 375-389. https://doi.org/10.1093/mnras/181.3.375

He, Y., Bayly, A. E., Hassanpour, A., Muller, F., Wu, K., & Yang, D. (2018). A GPU-based coupled SPH-DEM method for particle-fluid flow with free surfaces. *Powder Technology, 338*, 548-562. https://doi.org/10.1016/j.powtec.2018.07.043

He, Y. B., Laskowski, J. S., & Klein, B. (2001). Particle movement in non-Newtonian slurries: the effect of yield stress on dense medium separation. *Chemical Engineering Science, 56*(9), 2991-2998. https://doi.org/https://doi.org/10.1016/S0009-2509(00)00479-6

H. Hertz. (1882) “Uber die beruhrung fester elastischer korper (On the contact of elastic solids),” *J Reine Angew Math*, Vol. 92, pp. 156-171.

Ibrahim Dickey, R. D., Jackson, R. L., & Flowers, G. T. (2011). Measurements of the static friction coefficient between tin surfaces and comparison to a theoretical model. *Journal of Tribology, 133*(3). https://doi.org/10.1115/1.4004338

Jajcevic, D., Siegmann, E., Radeke, C., & Khinast, J. G. (2013). Large-scale CFD–DEM simulations of fluidized granular systems. *Chemical Engineering Science, 98*, 298-310. https://doi.org/10.1016/j.ces.2013.05.014

Kloss, C., Goniva, C., König, A., Amberger, S., & Pirker, S. (2012). Models, algorithms and validation for opensource DEM and CFD-DEM. *Progress in Computational Fluid Dynamics, 12*, 140-152. https://doi.org/10.1504/PCFD.2012.047457

Li, L. (2022). Special issue on numerical modeling in civil and mining geotechnical engineering. *Processes, 10*(8). https://doi.org/10.3390/pr10081571

Li, Y., Xu, Y., & Thornton, C. (2005). A comparison of discrete element simulations and experiments for 'sandpiles' composed of spherical particles. *Powder Technology, 160*(3), 219-228. https://doi.org/10.1016/j.powtec.2005.09.002

Machač, I., Ulbrichová, I., Elson, T. P., & Cheesman, D. J. (1995). Fall of spherical particles through non-Newtonian suspensions. *Chemical Engineering Science, 50*(20), 3323-3327. https://doi.org/https://doi.org/10.1016/0009-2509(95)00168-5

Marinack, M. C., Musgrave, R. E., & Higgs, C. F. (2013). Experimental investigations on the coefficient of restitution of single particles tribology transactions, 56(4), 572-580. https://doi.org/10.1080/10402004.2012.748233

Mindlin, R.D. (1949) Compliance of elastic bodies in contact. *Transactions of the ASME, Journal of Applied Mechanics*, 16, 259-268.

Minkin, L., & Sikes, D. (2018). Coefficient of rolling friction - lab experiment. *American Journal of Physics, 86*(1), 77-78. https://doi.org/10.1119/1.5011957

Moreira, A. B., Leroy, A., Violeau, D., & Taveira-Pinto, F. d. A. (2020). Overview of large-scale smoothed particle hydrodynamics modeling of dam hydraulics. *Journal of Hydraulic Engineering, 146*(2). https://doi.org/10.1061/(asce)hy.1943-7900.0001658

Nguyen, G. T., Chan, E. L., Tsuji, T., Tanaka, T., & Washino, K. (2021). Resolved CFD–DEM coupling simulation using volume penalisation method. *Advanced Powder Technology, 32*(1), 225-236. https://doi.org/10.1016/j.apt.2020.12.004

Ohno, K., Nitta, T., & Nakai, H. (2017). SPH-based fluid simulation on GPU using verlet list and subdivided cell-linked list. 2017 Fifth International Symposium on Computing and Networking (CANDAR).

Okesanya, T., Kuru, E., & Sun, Y. (2020). A new generalized model for predicting the drag coefficient and the settling velocity of rigid spheres in viscoplastic fluids. *SPE Journal, 25*(06), 3217-3235. https://doi.org/10.2118/196104-PA

Park, S.-H., Jo, Y. B., Ahn, Y., Choi, H. Y., Choi, T. S., Park, S.-S., Yoo, H. S., Kim, J. W., & Kim, E. S. (2020). Development of multi-GPU–based smoothed particle hydrodynamics code for nuclear thermal hydraulics and safety: potential and challenges. *Frontiers in Energy Research, 8*. https://doi.org/10.3389/fenrg.2020.00086

Pashias, N., Boger, D. V., Summers, J. M., & Glenister, D. J. (1996). A fifty cent rheometer for yield stress measurement. *Journal of Rheology, 40*, 1179-1189.

Peng, C., Zhan, L., Wu, W., & Zhang, B. (2021). A fully resolved SPH-DEM method for heterogeneous suspensions with arbitrary particle shape. *Powder Technology, 387*, 509-526. https://doi.org/10.1016/j.powtec.2021.04.044

Peng, Z., Doroodchi, E., Luo, C., & Moghtaderi, B. (2014). Influence of void fraction calculation on fidelity of CFD-DEM simulation of gas-solid bubbling fluidized beds. *AIChE Journal, 60*(6), 2000-2018. https://doi.org/10.1002/aic.14421

Picabea, J., Maestri, M., Cassanello, M., Salierno, G., De Blasio, C., Cardona, M. A., Hojman, D., & Somacal, H. (2022). Validation of CFD-DEM simulation of a liquid–solid fluidized bed by

dynamic analysis of time series. *Particuology, 68*, 75-87. https://doi.org/10.1016/j.partic.2021.11.003

Platzer, F., & Fimbinger, E. (2021). Modelling pasty material behaviour using the discrete element method. *Multiscale Science and Engineering, 3*(2), 119-128. https://doi.org/10.1007/s42493-021-00064-7

Potvin, Y., Thomas, E., Fourie, A., & Australian Centre for, G. (2005). Handbook on mine fill. Australian Centre for Geomechanics Nedlands, Western Australia.

Rackl, M., & Hanley, K. J. (2017). A methodical calibration procedure for discrete element models. *Powder Technology, 307*, 73-83. https://doi.org/https://doi.org/10.1016/j.powtec.2016.11.048

Robb, D. M., Gaskin, S. J., & Marongiu, J.-C. (2016). SPH-DEM model for free-surface flows containing solids applied to river ice jams. *Journal of Hydraulic Research, 54*(1), 27-40. https://doi.org/10.1080/00221686.2015.1131203

Robinson, M., Luding, S., & Marco Ramaioli, M. (2013). Grain sedimentation with SPH-DEM and its validation.

Salamat, J., & Genç, B. (2023). Numerical simulation of granular flow in concrete batching plant via discrete element method. *The European Journal of Research and Development, 3*(2), 11-28. https://doi.org/10.56038/ejrnd.v3i2.219

Sandeep, C. S., Senetakis, K., Cheung, D., Choi, C. E., Wang, Y., Coop, M. R., & Ng, C. W. W. (2021). Experimental study on the coefficient of restitution of grain against block interfaces for natural and engineered materials. *Canadian Geotechnical Journal, 58*(1), 35-48. https://doi.org/10.1139/cgj-2018-0712

Stokes, G. G. (1844). On the effect of the internal friction of fluids on the motion of pendulums. Pitt Press. https://books.google.ca/books?id=C1PLzgEACAAJ

Trujillo-Vela, M. G., Galindo-Torres, S. A., Zhang, X., Ramos-Cañón, A. M., & Escobar-Vargas, J. A. (2020). Smooth particle hydrodynamics and discrete element method coupling scheme for the simulation of debris flows. *Computers and Geotechnics, 125*, 103669. https://doi.org/https://doi.org/10.1016/j.compgeo.2020.103669

Tsuji, Y., Kawaguchi, T., & Tanaka, T. (1993). Discrete particle simulation of two-dimensional fluidized bed. *Powder Technology, 77*(1), 79-87. https://doi.org/https://doi.org/10.1016/0032-5910(93)85010-7

Valdez-Balderas, D., Domínguez, J. M., Rogers, B. D., & Crespo, A. J. C. (2013). Towards accelerating smoothed particle hydrodynamics simulations for free-surface flows on multi-GPU clusters. *Journal of Parallel and Distributed Computing, 73*(11), 1483-1493. https://doi.org/10.1016/j.jpdc.2012.07.010

Valentik, L., & Whitmore, R. L. (1965). The terminal velocity of spheres in Bingham plastics. *British Journal of Applied Physics, 16*(8), 1197. https://doi.org/10.1088/0508-3443/16/8/320

Washino, K., Chan, E. L., Miyazaki, K., Tsuji, T., & Tanaka, T. (2016). Time step criteria in DEM simulation of wet particles in viscosity dominant systems. *Powder Technology, 302*, 100-107. https://doi.org/10.1016/j.powtec.2016.08.018

Wu, D., Chen, W., Glowinski, D., & Wheeler, C. (2020). Modelling mineral slurries using coupled discrete element method and smoothed particle hydrodynamics. *Powder Technology, 364*, 553-561. https://doi.org/10.1016/j.powtec.2020.02.011

762 Zhang, Y., & Li, L. (2023). Experimental study on the natural mixing behaviour of waste rocks poured in
763 a paste backfill. *International Journal of Mining, Reclamation and Environment*, 1-25.
764 https://doi.org/10.1080/17480930.2023.2235847

765 Zhang, Z., & Yin, T. (2018). A coupled CFD–DEM simulation of slurry infiltration and filter cake
766 formation during slurry shield tunneling. *Infrastructures, 3*(2).
767 https://doi.org/10.3390/infrastructures3020015

768 Zhao, J., & Shan, T. (2013). Coupled CFD–DEM simulation of fluid–particle interaction in geomechanics.
769 *Powder Technology, 239*, 248-258. https://doi.org/10.1016/j.powtec.2013.02.003

770 Zhao, T., Houlsby, G. T., & Utili, S. (2014). Investigation of granular batch sedimentation via DEM–CFD
771 coupling. *Granular Matter, 16*(6), 921-932. https://doi.org/10.1007/s10035-014-0534-0

772 Zhou, S., & Li, L. (2022). Numerical investigation on the impact of tailings slurry on catch dams built at
773 the downstream of a breached tailings pond. *Processes, 10*(5). https://doi.org/10.3390/pr10050898

774 Zhu, H. P., Zhou, Z. Y., Yang, R. Y., & Yu, A. B. (2008). Discrete particle simulation of particulate systems:
775 A review of major applications and findings. *Chemical Engineering Science, 63*(23), 5728-5770.
776 https://doi.org/10.1016/j.ces.2008.08.006